Journal of Electroanalytical Chemistry 736 (2015) 61–68

Contents lists available at ScienceDirect

Journal of Electroanalytical Chemistry

journal homepage: www.elsevier.com/locate/jelechem

In-situ Mg^{2+} release monitored during magnesium alloy corrosion

Philippe Dauphin-Ducharme [a], R. Matthew Asmussen [b], David W. Shoesmith [b], Janine Mauzeroll [a,*]

[a] Laboratory for Electrochemical Reactive Imaging and Detection of Biological Systems, Department of Chemistry, McGill University, Montreal, QC H3A 0G4, Canada
[b] Department of Chemistry and Surface Science Western, Western University, London, Ontario N6A 5B7, Canada

ARTICLE INFO

Article history:
Received 12 September 2014
Received in revised form 22 October 2014
Accepted 26 October 2014
Available online 1 November 2014

Keywords:
Magnesium alloy
Ion-selective electrodes
Potentiometric sensor
Microstructure distribution
Magnesium corrosion

ABSTRACT

Quantitative *in-situ* and localized analytical methods that can monitor Mg^{2+} release are central to probe the impact of the microstructure on magnesium alloy corrosion. As such, a potentiometric micro-Mg^{2+} ion-selective membrane electrode is fabricated, calibrated, characterized and used to selectively monitor the Mg^{2+} release from different cast Mg AM50 alloys during corrosion. We demonstrate that the local Mg^{2+} release is tied to the alloy microstructure and its aluminum distribution, indicating a possibility of optimization of the base material corrosion properties.

1. Introduction

Decreasing vehicle weight in the automotive industry is an ever-growing trend. As such, one of the most promising avenues under examination is the use of Mg alloys, the lightest viable structural metal for commercial applications [1,2]. The application of Mg-based components in automobiles is challenging not only because of the required mechanical properties (i.e. ductility) but also due to the poor corrosion performance that plagues Mg alloy use in external components. These alloys have been employed to date as door frames, lift-gates, front-end structures and many cabin components.

The Mg corrosion mechanism can be generally described by three reactions, Eqs. (1)–(3):

$$Mg \rightarrow Mg^{2+} + 2e^- \quad (1)$$

$$2H_2O + 2e^- \rightarrow 2OH^- + H_2 \quad (2)$$

$$Mg^{2+} + 2OH^- \leftrightarrows Mg(OH)_2 \quad (3)$$

The anodic dissolution of Mg (Eq. (1)) in aqueous environments is coupled to the reduction of water (Eq. (2)). As a result, in unbuffered solutions, a pH increase occurs in the immediate vicinity of the surface leading to deposition of a porous corrosion product, $Mg(OH)_2$ ($K_{sp} = 5.61 \times 10^{-12}$) [3], on the corroding surface (Eq. (3)). This deposited layer has protective properties in high alkaline environments [4] but does not act as an effective corrosion barrier at pH < 12. However, its accumulation as a porous layer on the alloy surface may eventually hamper the release of Mg^{2+}.

An extensive catalog of Mg alloys is available commercially, each alloy tailored to produce specific physical properties. Their corrosion performance can be improved through casting modifications [5] that alter the secondary phase distribution within the alloy [6]. For this study, the AlMn-containing AM50 Mg alloys were used since they are commercially available and commonly utilized as automotive components [7]. Al is the most common alloying addition to Mg alloys to improve physical properties such as hardness and castability as well as to improve corrosion resistance. Mn is utilized to scavenge contaminants (Fe, Ni, Cu) in the molten alloy limiting their presence in the cast material as they are highly detrimental to corrosion resistance [8]. With these alloying additions, this series of Mg alloys is comprised of a Mg-rich α-phase, $Mg_{17}Al_{12}$ β-phase, and AlMn intermetallics (Fig. 1) [1,9–12].

The corrosion of Mg alloys is complex due to the influence of microgalvanic coupling between these phases. The β-phase and AlMn intermetallics are more cathodic than the α-Mg matrix (~97 at.% Mg) [13] and, thus, capable of forming galvanic couples with the α-Mg. There exist contradictions in the literature since both the β-phase [14] and the AlMn intermetallics [15] have been reported as the dominant cathode in microgalvanic coupling. It has also been reported that the β-phase can act as a barrier against corrosion [16]. A schematic representation of this microgalvanically coupled process is shown in Fig. 1, where Mg^{2+} is anodically dissolved from the α-Mg grains (Eq. (1)) coupled to the cathodic reduction of water (Eq. (2)) on the β-phase and/or AlMn intermetallics.

* Corresponding author. Tel.: +1 (514) 398 3898; fax: +1 (514) 398 3797.
E-mail address: janine.mauzeroll@mcgill.ca (J. Mauzeroll).

http://dx.doi.org/10.1016/j.jelechem.2014.10.030
1572-6657/

Given the wide range of alloying elements, compositions, and microstructures in Mg alloys, there is a clear need to develop quantitative analytical methods to investigate their influence on Mg alloy corrosion. The ability to selectively, and quantitatively, track *in-situ* the species released during corrosion, such as Mg^{2+}, OH^-, and H_2 would be a major advantage in monitoring the corrosion of Mg alloys. Such *in-situ* methods would complement *ex-situ* analyses as scanning electron microscopy (SEM), confocal scanning laser microscopy, transmission electron microscopy and X-ray energy dispersive spectroscopy (XEDS), which have been used extensively to characterize Mg alloys before and after corrosion [17–19].

There are several techniques capable of high spatial resolution *in-situ* tracking of corrosion including scanning Kelvin probe microscopy [18], the scanning vibrating electrode technique [20,21], localized impedance spectroscopy [22], and scanning electrochemical microscopy (SECM). Recently SECM, using an ion-selective microelectrode, was applied to determine the concentration distributions of Zn^{2+} during either Zn/Fe galvanic corrosion or Zn dissolution [23,24]. Nazarov et al. developed Na^+ and Cl^- ion-selective electrodes to monitor the distribution of NaCl during the corrosion of a Al–Zn coated steel [25]. Sb or pH-selective microelectrodes have been used to measure H^+ distribution during the corrosion of silver iodide-based solid-state electrodes in cyanide solution [26] and Al-rich coated steels [27]. Etienne and co-workers used the potentiometric and constant-distance modes of SECM to image dissolving calcite crystals using Ca^{2+} ion-selective microelectrodes [28]. Ion-selective microelectrodes for Mg^{2+} have been used to investigate Mg alloy corrosion. Lamaka et al. used an ion-selective microelectrode (2 μm aperture) fabricated using a neutral ionophore ETH 1907 [29] and ETH 5214 [30], to image the Mg^{2+} release from a scratched AZ31 alloy, while Souto et al. were able to monitor release from AZ63 alloys [31]. A synthetic malonamide derivative was used as an ionophore by Izquierdo et al. to assess the local corrosion of AZ31 [32] and the galvanic corrosion of pure Mg [33].

To date, SECM studies of Mg^{2+} release have not been applied to correlate the differences in corrosion rate caused by alterations in alloy microstructure [34,35]. In this study, we report the development, calibration and characterization of a 500 nm aperture micro-Mg^{2+} potentiometric sensor that is sensitive to variations in Mg^{2+} release resulting from differences in the distribution of secondary phases. This smaller micro-Mg^{2+} sensor has, a low detection limit, good selectivity towards Mg^{2+} due to the use of a different ionophore (ETH 7025). In this study, the micro-Mg^{2+} sensor is prepositioned close to the Mg alloy using the shear-force signal of our scanning electrochemical microscope and used to record chronopotentiometric curves during alloy corrosion. Chronopotentiometric measurements were preferred over SECM imaging in order to control the initiation time corrosion over multiple sampled areas of the alloys. Using corroborating results based on SEM and XEDS imaging, we observed a clear correlation between the size of microstructural features and the resulting corrosion performance of the alloy.

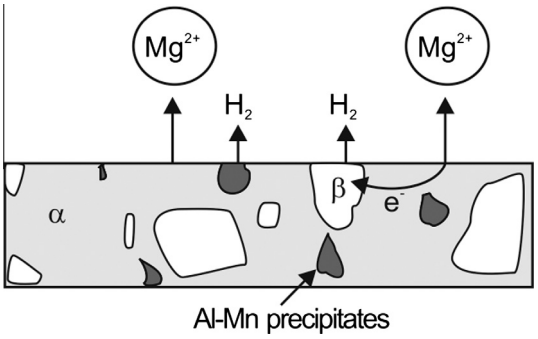

Fig. 1. Schematic representation of a heterogeneous AM Mg alloy surface showing the α- and β-phases and the AlMn precipitates. The β-phase and AlMn precipitates are shown acting as cathodes for water reduction/H_2 production microgalvanically-coupled to the anodically dissolving α-phase.

2. Experimental section

2.1. Micro-Mg^{2+} sensor fabrication

Quartz capillaries (0.3 mm internal diameter (ID), 1 mm outer diameter (OD), Sutter Instrument, Novato, CA) were washed for 2 h in 0.1 M HNO_3, dried and pulled with a P-2000 CO_2 laser puller (Sutter Instrument) to 500 nm aperture and taper distance (distance measured from the tip of the microcapillaries to ID = 0.15 mm) of 2.04 mm. The pulling program is reproducible within 4% based on the optically measured taper distances. To silanize the pulled pipettes, adhesive putty was used to secure the pipettes bottom-up on the side of a vial containing 50 μL of dimethyldichlorosilane (Fluka, St. Louis, MO), which was heated to 40 °C for 30 min. The pipettes were subsequently baked for 2 h at 250 °C to initiate hydrolysis. Pipettes were then backfilled with a 10 mM $MgCl_2$ (Acros, New Jersey) aqueous solution (Millipore MilliQ 18.2 MΩ water).

2.2. Ion-selective membrane preparation

Magnesium ionophore, N,N′,N″-tris[3-(heptylmethylamino)-3-oxopropionyl]-8,8′-iminodioctylamine (ETH 7025), potassium tetrakis(4-chlorophenyl) borate (KT*p*ClPB), *o*-nitrophenyl-*n*-octylether (*o*-NPOE), high molecular weight poly(vinylchloride) (PVC) and cyclohexanone were purchased from Fluka (St. Louis, MO). An ion-selective membrane solution (ISMS) was prepared by mixing ETH 7025: 10.3 wt.%, KT*p*ClPB: 9.2 wt.%, *o*-NPOE: 80.5 wt.%. Following the preparation of this mixture, PVC: 12 wt.% of the total desired membrane quantity and cyclohexanone: 3 times the weight of the total membrane were added [36]. ETH 7025, KT*p*ClPB, *o*-NPOE and PVC were dissolved in cyclohexanone since it has been previously reported that cyclohexanone offers a good compromise between evaporation time and solubility compared to tetrahydrofuran (THF), which leads to holes within the membrane, inhibiting conduction [37]. The mixture was left to dissolve for ~12 h. Following synthesis of the ion-selective membrane, infrared characterization was carried out to verify the ionophore ability to effectively bind Mg^{2+} ions using a Platinum ATR QuickSnap FT-IR spectrometer (A220/D-01, Bruker).

2.3. Micro-Mg^{2+} sensor fabrication

The tip of the back-filled pipette was dipped (~30 s) in the ISMS until a column of solution of 100 μm forms at the end. The pipettes were set aside overnight to allow cyclohexanone to evaporate in air. The homogeneity of the ion-selective membrane at the tip of the pipettes was examined using a Zeiss NVision 40 dual beam microscope, operated in scanning electron microscopy mode at 5 kV accelerating voltage. Following the membrane insertion, a Ag|AgCl (0.125 mm diameter – GoodFellow Metals, Huntingdon, England) wire, prepared following a published procedure [38] was connected to a gold pin using silver conductive epoxy (H20E kit – Paisley Products of Canada Inc., Ville St-Laurent, Canada). An additional borosilicate glass (ID: 1.16 mm, OD: 2.00 mm; Sutter Instrument) was used to increase the overall robustness of the sensor. The micro-Mg^{2+} sensor was conditioned in 10 mM $MgCl_2$

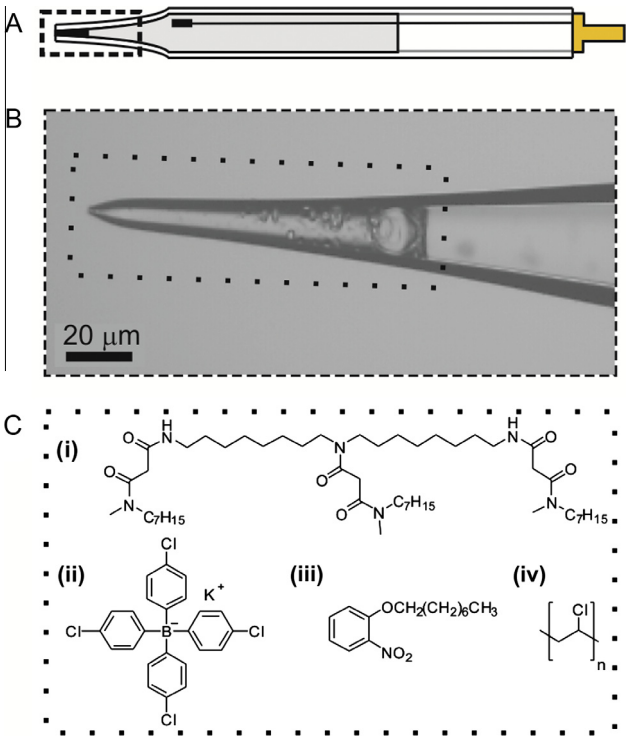

Fig. 2. (A) Schematic representation of the micro-Mg^{2+} sensor, where the grey lines represent the silanized internal void and the black lines, the ISM; (B) optical micrograph of the micro-Mg^{2+} sensor with the membrane inserted; (C) molecular structures of the ISMS composition inserted at the tip of the pipette: (i) ETH 7025: N,N′,N″-tris[3-(heptylmethylamino)-3-oxopropionyl]-8,8′-iminodioctylamine; (ii) KT*p*ClPB: Potassium-tetrakis(*p*-chlorophenyl)-borate; (iii) *o*-NPOE: *o*-nitrophenyl-*n*-octylether; (iv) PVC: poly(vinylchloride).

solution for 24 h to allow equilibration of the ionophore in the polymeric membrane.

2.4. Electrochemical characterization and corrosion measurements

The ISM ohmic resistance was measured using a voltage divider circuit (see Fig. S1 in the supplemental information) in order to compare response times with literature results. The voltmeter used (Solartron 7065 Microprocessor Voltmeter) requires an input impedance higher than 1 GΩ to obtain an accurate measurement.

The micro-Mg^{2+} sensors were calibrated using eight different solutions of $MgCl_2$ ranging from 10^{-8} to 10^{-1} M. Open circuit potentials (OCP) were recorded against a standard saturated calomel electrode (SCE – REF451: Radiometer analytical, Lyon, France) for 5 min to ensure a stable potential response. The OCP measurements were performed using an ElProScan 1 system (HEKA, Germany; model PG340).

Following analytical calibration and electrochemical characterization, the micro-Mg^{2+} sensor was used to monitor *in-situ* Mg^{2+} fluxes during the corrosion of a Mg alloy. Sand cast and graphite cast AM50Mg alloy rods and die cast AM50 Mg alloy plates were received from General Motors (Canada). The sand and graphite cast alloys were machined into 1.5 cm × 1.5 cm × 1 cm samples, while the die cast alloy was machined into 1.5 cm × 1.5 cm × 0.2 cm samples. The alloys complied with the ASTM B275 standard for this alloy (see the inductively coupled plasma (ICP) results in Table S1) [39]. The samples were mounted in Struers Epo-Fix epoxy to expose a single face of the sample and polished to a mirror finish following a published procedure [20]. The polished alloy samples were imaged in back scattered electron mode (BSE) using a LEO 440 SEM or Hitachi 3400-N variable pressure SEM both equipped with a Quartz XONE XEDS system. The surface coverages of cathodic sites was determined with Image-Pro Plus® software.

The micro-Mg^{2+} sensor was approached towards the Mg alloy surface in air using shear force methodology [40] (stimulation amplitude, 1 V; stimulation frequency, 286.7 kHz) to determine the tip-to-substrate distance prior to solution exposure. A 50 μL drop of 1.6 wt.% NaCl (ACP, Montreal) solution was deposited on the AM50Mg alloy surface at the same location where the micro-Mg^{2+} sensor was pre-positioned, to initiate corrosion and the release of Mg^{2+}. The average surface coverage of the NaCl solution drop is ~100 mm^2. A Ag|AgCl reference electrode was used during corrosion measurements. To monitor the Mg^{2+} ion release, the OCP of the sensor was recorded over time and converted to the SCE scale. A petri dish filled with water was placed next to the experimental setup to make sure that negligible evaporation of the drop (<0.5 μL) occurred over the course of the experiment (<1.2 h).

3. Results and discussion

3.1. Ion-selective membrane (ISM) affinity towards Mg^{2+} ions

In the fully assembled micro-Mg^{2+} sensor (Fig. 2A), the tip of the silanized pipette contains ~100 μm ISM (Fig. 2B). The components of the ISM (Fig. 2C) include the (i) ionophore, (ii) KT*p*ClPB, which reduces the anionic interferences, equilibrates charge induced by the capture of Mg^{2+} to insure permselectivity, and increases sensor lifetime, (iii) *o*-NPOE that forms a solidified gel with (iv) PVC, which is added to increase the mechanical strength of the membrane [41].

The SEM micrographs in Fig. 3A and B show a 500 nm aperture size was typical for the laser-pulled pipettes. The overall homogeneity of the ISM was also characterized using SEM (Fig. 3C).

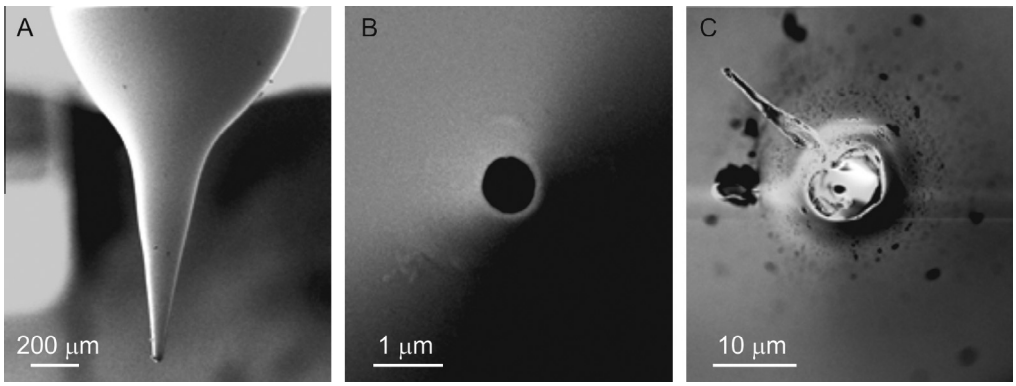

Fig. 3. SEM characterization of the micro-Mg^{2+} sensor; (A) side view of the sensor, and the pipette prior to (B) and after (C) insertion of the ISM at the tip.

Polymer-based ion-selective electrodes rely on the selective binding of an ionophore to a target ion. Our micropipette sensor used ETH 7025 as an ionophore to selectively bind to Mg^{2+} hard cations. The twelve lone pairs bared at the amide groups present in its chemical structure donate electron density to form an octahedral complex with Mg^{2+} [42]. When folded, the number of atoms separating each electron-rich site is well matched with the radii of Mg^{2+}. Following membrane assembly, the ionophore activity towards Mg^{2+} ions was investigated using infrared spectroscopy (IR) (see Fig. S2 in supplemental information). The dried polymer membrane presents two peaks (ν = 1610 and 1525 cm^{-1}) corresponding to C=O bonds stretching vibration within the amide groups found within the ionophore chemical structure. The polymeric membrane was then conditioned in a drop of 0.1 M of $MgCl_2$ and a second infrared spectrum acquired. A new C=O stretching peak (ν = 1750 cm^{-1}) corresponding to a weaker bond, indicative of an efficient binding of Mg^{2+} to the ionophore, appeared in the spectra. Our results are consistent with other IR studies of similar coordination ligands with ETH 7025; for example, the acetylacetonate (acac) ligand shows a shift to higher wavenumbers upon coordination to metal centers [43,44].

During the *in-situ* monitoring of Mg^{2+}, the dipole-ion interaction is a dynamic process, where Mg^{2+} binds and unbinds the ionophore at equilibrium [42]. The membrane potential measured by the sensor will vary as a function of the number of binding events occurring at the interface with the external solution given the constant activity of the $MgCl_2$ internal solution.

3.2. Micro-Mg^{2+} sensor calibration and selectivity

The micro-Mg^{2+} sensor was calibrated over a large range of Mg^{2+} activity (Fig. 4).

The dynamic range, detection limit, response time [45] and overall sensitivities of the micro-Mg^{2+} sensor were analytically validated at a 95% confidence level for 20 working micro-Mg^{2+} sensors over two weeks as reported in Table 1.

The dynamic range (−5.7 to −1.4 (in $\log a_{Mg^{2+}}$)) offers a wide activity range over which Mg^{2+} release can be monitored *in-situ* during Mg alloy corrosion. For example in a previous study, when a current of 6 mA cm^{-2} was applied to a Mg alloy, following a 1 h exposure to a 1 N NaCl solution of pH = 11, a solution concentration of 10^{-3} M for Mg^{2+} was obtained using weight loss measurements, which is located well within the measured dynamic range of the sensor [46]. A sensitivity (slope of the electrode response) of 23 ± 1 mV/decade and a detection limit of −5.8 ± 0.2 were obtained. A similar sensitivity (25.5 ± 0.5 mV/decade) and detection limit (−4.8 ± 0.2) can be found in the literature [37]. The detection limit was determined from the extrapolated intercept of the two linear portions of the calibration curve (Fig. 4) [47]. As an example in Fig. 4, the first linear portion was set between 10−8 and 10−6 M while the second one was set between 10−5 up to 10−1 M. An ISM ohmic resistance (see Table 1) of 20 ± 5 GΩ was measured and is similar to the reported literature value (34 ± 6 GΩ) [37]. Thus, regardless of its micron scale dimensions, the analytical response of the micro-Mg^{2+} sensor was on a par with similar larger sensors [37].

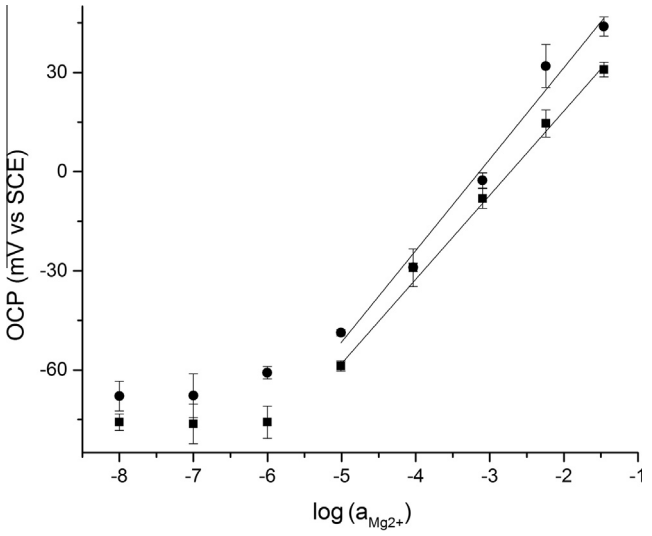

Fig. 4. Calibration curve for the micro-Mg^{2+} sensor using 8 solutions of $MgCl_2$ ranging from 10^{-8} to 10^{-1} M after fabrication (■) and 2 weeks usage (●). Linear regression equation: (■) $y = 25.1x + 69.6$ with a correlation coefficient (R^2) value of 0.996 (●) $y = 27.6x + 7.0$ with a correlation coefficient (R^2) value of 0.978: error bars represents a 95% confidence level.

Due to interference effects, the micro-Mg^{2+} sensor exhibited a non-Nernstian slope of 23 ± 1 mV/decade (n = 20), compared to the theoretical Nernstian response of 29.1 mV/decade (z_a = 2). For that reason, and to calibrate the sensor under conditions which simulate anticipated corrosion conditions, a fixed interference method was used to measure selectivity coefficients [47] with the activity of the interfering ion (a_b) fixed while varying the activity of the principal ion (a_a). A new calibration curve was prepared and the detection limit for a_a determined as the intersection between the extrapolated linear portions. Using Eq. (4), the selectivity coefficient ($k^{pot}_{a,b}$) was calculated for Na^+ (1.6 wt.%), Ca^{2+} (0.1 wt.%) and OH^- (pH = 9.74).

$$K^{pot}_{a,b} = a_a/(a_b)^{z_a/z_b} \quad (4)$$

The [Na^+] and [Ca^{2+}] chosen were based on the simulated exposure environment specified by General Motors Canada while the pH was that measured after 2 h of exposure of the graphite cast alloy to a 1.6 wt% NaCl solution. In Table 1, the large negative values of $k^{pot}_{Mg^{2+},Na^+}$ (−4.0 ± 0.4 (n = 3)) and $k^{pot}_{Mg^{2+},OH^-}$ (−12.9 ± 0.9 (n = 3)), indicate that the ISM electrochemical response was not influenced by the presence of Na^+ and OH^-. In contrast, the value reported in Table 1 for Ca^{2+}, a $k^{pot}_{Mg^{2+},Ca^{2\pm}} = -0.3 \pm 0.8$ confirms Ca^{2+} as a potential interfering species and corroborates results obtained in a study not focused on corrosion [37]. Although Ca^{2+} can interfere with the ISM, its contribution to the signal can be removed using the measured selectivity coefficient should the corroding environment contain Ca^{2+}.

3.3. Microstructural analysis of the sand, graphite and die cast alloys

In Table 2, we report the surface coverage by potential cathodic features (β-phase and AlMn intermetallics) and the average β-phase size obtained for the three Mg alloys.

Due to their heterogeneous nature, all three alloys have a similar surface coverage by potential cathodes ranging from 1.5% to 7.2% depending on the specific region observed on the alloy surface. Although the approximate cathodic surface coverages were similar, the size of the β-phase was different. As observed in Fig. 5A–C, the β-phase features on the sand cast (20–25 μm on the longest axis) were larger than those on the graphite cast (~10 μm) and die cast Mg alloys (0.2–0.5 μm). This dichotomy has consequences in terms of Al distribution which is more confined in discrete β-phase precipitates in the sand cast alloy while, in the graphite and die cast alloys, a more homogeneous distribution is observed in the XEDS maps, Fig. 5D–F.

A further estimate of the amount of β-phase content (in wt.%) of the three AM50 cast alloys can be obtained using FactSage numerical simulation software. This analysis is based on a knowledge of

Table 1
Micro-Mg^{2+} sensor potentiometric properties. Figures of merit are all expressed at a 95% confidence interval.

Slope of the electrode response (mV/decade)	Detection limit ($\log a_{Mg^{2+}}$)	Dynamic range ($\log a_{Mg^{2+}}$)	Selectivity coefficients $\left(\log K^{pot}_{Mg,X}\right)$			Response time ($t_{95\%}$, s)	Membrane ohmic resistance (GΩ)
			X = Na^+	X = Ca^{2+}	X = OH^-		
23 ± 1 (n = 20)	−5.8 ± 0.2 (n = 20)	−5.7 to −1.4	−4.0 ± 0.4 (n = 3)	−0.3 ± 0.8 (n = 3)	−12.9 ± 0.9 (n = 3)	1.7 ± 0.3 (n = 6)	20 ± 5 (n = 6)

Table 2
Relative surface coverage by β-phase and AlMn intermetallics and their respective average sizes in the sand, graphite and die cast surfaces.

Sample	β-phase and intermetallics (cathode) coverage (%)	β-phase size (μm)
Sand cast	1.56–7.2	20–25
Graphite cast	1.5–6	10
Die cast	2.9–5.7	0.2–0.5

Table 3
Microstructural features and their respective weight percentages calculated using FactSage for the three AM50Mg alloys.

	α-phase (wt.%)	β-phase ($Mg_{17}Al_{12}$) (wt.%)	Intermetallics (Al_8Mn_5) (wt.%)
Sand cast	95.46	4.10	0.37
Graphite cast	95.63	3.83	0.47
Die cast	94.54	4.97	0.40

the alloy composition, determined by inductively coupled plasma (ICP) analyses (Table S1), and Scheil equilibrium cooling calculations for the casting process [48,49]. The calculated amounts of β-phase in the three cast alloys are 4.97 wt.% (die cast), 4.10 wt.% (sand cast) and 3.83 wt.% (graphite cast), Table 3. This trend can be correlated to the combination of compositional changes and cooling rates, the lower wt.% of β-phase being dictated by the faster cooling rate. However, no similar trend was observed for the AlMn intermetallics, where wt.% fractions vary from 0.4 wt.% to 0.37 wt.% up to 0.47 wt.% for the die, sand and graphite cast alloys, respectively.

The analyses show the complexity in identifying microstructural differences between Mg alloys. Since the release of Mg^{2+} is correlated directly to corrosion rate and amount of corrosion products deposited (see Eqs. (1) and (3)), any observed trend in Mg^{2+} release can be correlated to one of the listed trends as a mean of identifying the major microstructural influence. This approach would be directly applicable in an industrial setup for identification of corrosion behavior differences based on artifacts resulting from casting processes.

3.4. In-situ Monitoring of Mg^{2+} during corrosion of AM50 sand, graphite and die cast alloys

The micro-Mg^{2+} sensor was pre-positioned in air using the shear force module of the SECM. In Fig. 6A, a schematic of the shear force module is shown where stimulation and receiver piezoelectric actuators are mounted and screwed on the micro-Mg^{2+} sensor. An electrical pulse is applied to the stimulation piezoelectric actuator to induce the mechanical vibration of the sensor. Amplitude and phase modulation of a resonance frequency of the vibrating sensor is recorded at the receiver piezoelectric actuator and used to regulate the sensor-to-Mg alloy distance. Pre-selection of a working resonance frequency (which is distance sensitive) is performed according to known literature [40] and reported in Fig. S3. In Fig. 6B, at 286.7 kHz, a ~50% amplitude damping was observed and was chosen as the working shear force frequency. The retraction and approach curves acquired at 286.7 kHz, presented in Fig. 6C, demonstrate that as the micro-Mg^{2+} sensor entered the shear force regime (0.5 μm), a decrease in the amplitude gradually occurred as the sensor-to-Mg alloy distance decreased until the point of lowest amplitude (0.22 μm) where

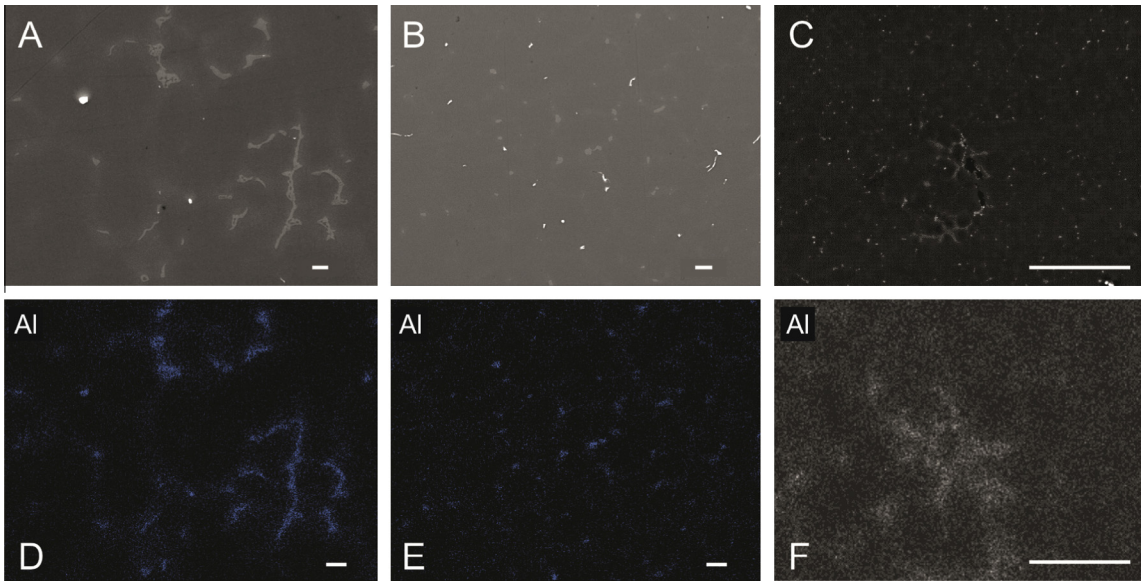

Fig. 5. SEM micrographs of polished (A) sand cast, (B) graphite cast, and (C) die cast alloy surfaces: (D)–(F), the corresponding XEDS maps showing the Al distribution. All scale bars correspond to 20 μm.

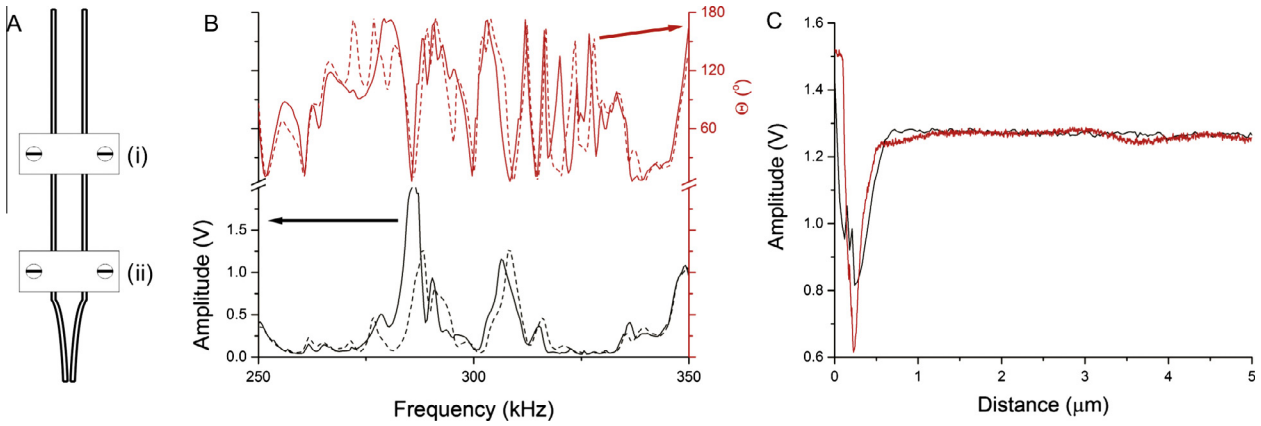

Fig. 6. Determination of the micro-Mg^{2+} sensor distance from the corroding surface; (A) shear force setup schematic where (i) and (ii) represent the stimulation and receiver piezos, respectively; (B) shear force spectra in amplitude (black curve) and phase (red curve) taken when the micro-Mg^{2+} sensor was placed far from the surface (full line) and when it touches the surface (dash line). Determination of the working frequency applied at the stimulation piezo (286.7 kHz); (C) approach (black line) and retraction (red line) curves recorded in amplitude at 1 μm/s and 3 nm/s, respectively.

the sensor gently touched the Mg alloy surface. Therefore, the micro-Mg^{2+} was prepositioned 50 μm from the surface using shear force with high precision (1 nm) to avoid any convection from the H_2 evolution and remain within the dynamic range of the sensor.

Fig. 7A presents a schematic representation of a 50 μL drop of a 1.6 wt.% NaCl solution placed on a corroding AM50 alloy surface. A Ag|AgCl reference electrode was placed in the droplet and the OCP of the sensor recorded with time. Using the calibration curve (Fig. 4), the OCP values can be expressed as $\log(a_{Mg^{2+}})$. All the activities measured using the micro-Mg^{2+} sensor were within the dynamic range of the sensor (Fig. 4) and therefore analytically valid. A sharp increase in Mg^{2+} activity was observed at the beginning of the corrosion process. With time, the rate of increase in activity decreased and the activity itself stabilized after 1–1.2 h of exposure, Fig. 7B. The overall release profile is consistent with the expected corrosion of Mg. During the initial stages (<20 s), intense dissolution of the alloy is observed. Assuming that the release of 1 mol of Mg^{2+} results in the generation of 2 mol of OH^- Eqs. (1) and (2), within this initial timeframe, the $a_{Mg^{2+}}$ surpassed the solubility limit of $Mg(OH)_2$, leading to deposition of corrosion product on the alloy surface, and a decrease in Mg dissolution rate. Under these conditions Mg^{2+} release is thought to be controlled by its diffusion through the thickening corrosion product layer [50]. For exposure times >1 h, the rate of Mg^{2+} release decreases. Replicate measurements using four different micro-Mg^{2+} sensors above sand cast AM50 alloy samples, Fig. 7C, lie within the same activity domain.

In-situ quantitative monitoring of Mg^{2+} using the sensor reveals a higher a_{Mg2+} release from the sand cast compared to the graphite cast which, in turn, is higher than that from the die cast alloy. A $\log(a_{Mg^{2+}})$ of −1.03 for sand cast, −1.85 for graphite cast and -2.33 for die cast, respectively were recorded at $t = 1$ h, Fig. 7B. As such, following 1 h immersion, corrosion rates of 2.72 mg/cm^2/d for the sand cast, 0.41 mg/cm^2/d for the graphite cast and 0.11 mg/cm^2/d for the die cast are calculated using the solution volume, area under the drop and exposure time. These measured differences in Mg^{2+} release arise from the microstructural differences between the alloys. The three alloys have similar cathodic surface coverages (β-phase and AlMn precipitates, Table 2), and only small differences in their β-phase content (Table 3). However, the distribution of Al within the alloy varies between the three casts. The sand cast, with a larger average β-phase size (Table 2)

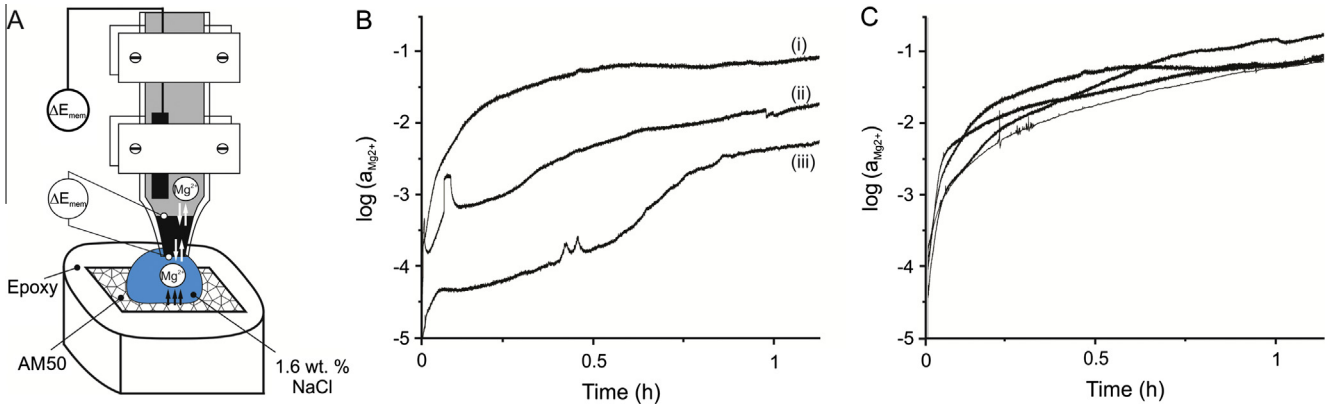

Fig. 7. (A) Schematic representation of a AM50Mg alloy mounted in epoxy with a drop of 1.6 wt.% NaCl solution emplaced to allow measurement of the release of Mg^{2+} with the micro-Mg^{2+} sensor mounted with shear force piezoelectric elements. The Mg^{2+} ions equilibrates at the exterior and interior walls of the ISM giving rise to a difference in junction potential (ΔE_{mem}) recorded at the Ag|AgCl wire; (B) $\log(a_{Mg^{2+}})$ (obtained from OCP measurements using the calibration curve in Fig. 4) measured over the sand (i), graphite (ii) and die (iii) cast alloy surfaces for ~1.2 h. The micro-Mg^{2+} sensor was placed 50 μm from the surface: (C) $\log(a_{Mg^{2+}})$ (from OCP values) measured over the sand cast alloy for ~1.2 h. The micro-Mg^{2+} sensor was placed at 50 μm away from the surface. The four different curves represent four different samples where the Mg^{2+} ions release was monitored using four different micro-Mg^{2+} sensors. All $\log(a_{Mg^{2+}})$ measured have been corrected for drop volume loss (measured using a micro volume syringe) occurring during the experiment (<5 μL for the most active sand cast sample).

congregates a larger amount of Al in the β-phase, while the die cast with smaller β-phase size, has a more even distribution throughout the alloy surface (Fig. 5).

It could be concluded from this study that the Al distribution of the Mg alloys plays a critical role in their corrosion behavior. The evenness of the Al distribution is in the order:

Sand cast < graphite cast < die cast

This trend is the inverse of the rate and extent of Mg^{2+} release measured by the micro-Mg^{2+} sensor. A recent report showed differences in corrosion rate and damage morphology between the sand cast, graphite cast and die cast AM50 alloy, induced by the differences in the microstructure size [35]. The corrosion rate is in the order: sand cast > graphite cast > die cast, which correlates directly with the release of Mg^{2+} measured with the micro-Mg^{2+} sensor, and confirms the influence of microstructure and Al distribution on the corrosion behavior of these alloys.

Compared with corrosion rates calculated from mass loss measurements following long immersion times (24–96 h) [35], the micro-Mg^{2+} sensor has the ability to rapidly determine corrosion rates through Mg^{2+} release *in-situ* and capture the event over short times (1.7 s). For example, the initial corrosion rates measured by the micro-Mg^{2+} sensor on the sand cast (2.72 mg/cm^2/d vs. 0.90 mg/cm^2/d) is initially larger and can be attributed to the creation of extensive corrosion events known to initiate during early immersion [17]. The rates on the graphite cast (0.41 mg/cm^2/d vs 0.70 mg/cm^2/d) and die cast (0.11 mg/cm^2/d vs. 0.22 mg/cm^2/d) are comparable to one another, with the minor discrepancies resulting from an accumulation of corrosion product ($Mg(OH)_2$) on the alloy surface.

Additionally, the profiles in Fig. 7B show distinct differences in the evolution of the corrosion process for the three different casts, confirming that this mode of application of SECM can be used to perform real time monitoring of the influence of microstructure on Mg alloy corrosion. Our previous studies of the corrosion performance of these alloys [17,35], based on the analysis of the distribution of corrosion damage using the *ex-situ* technique of confocal laser scanning microscopy, are consistent with the profiles shown in Fig. 7B, but provide only limited real time information. These previously published studies showed the rapid development of extensively corroded sites on the sand cast alloy consistent with the rapid and continuous release of Mg^{2+} as detected by the sensor, Fig. 7B. By contrast, the accumulation of damage on the die cast alloy was considerably slower and more widely distributed which is also consistent with the relatively slow release of Mg^{2+} detected by the sensor over the first 30 min of exposure.

4. Conclusion

A combination of *ex-situ* and *in-situ* techniques have been applied to investigate the corrosion process on three casts (sand, die, graphite) of the AM50 alloy.

A 500 nm potentiometric micro-Mg^{2+} sensor was characterized using SEM and ohmic resistance measurements, and analytically validated through a calibration curve and selectivity study of the ISM.

The micro-Mg^{2+} sensor possessed a large dynamic range, good selectivity towards Mg^{2+}, and could be prepositioned with high resolution with respect to the substrate surface.

This sensor was used to monitor Mg^{2+} release from the corroding surfaces of the three casts. The sensor detected Mg^{2+} release which increased in the order, sand cast > graphite cast > die cast.

These measurements correlated with a decrease in size of the β-phase and with an increase in Al distribution in the alloys. This sensitivity to small microstructural variations allows the real-time tracking of Mg^{2+} release through the stages of the corrosion process; a rapid initial release, a decrease due to the accumulation of a $Mg(OH)_2$ deposit, and a final stage controlled by Mg^{2+} diffusion through the porous $Mg(OH)_2$ layer.

This sensor can be reliably applied to monitor the corrosion process on a range of Mg alloys.

Conflict of interest

The authors declare no conflict of interest to this work.

Acknowledgements

This work was supported in part by the Natural Sciences and Engineering Research Council of Canada (NSERC) and General Motors of Canada. We would like to acknowledge Dr. Mohsen Danaie and Prof. Gianluigi A. Botton for performing electron microscopy of the micro-Mg^{2+} sensor and expertise inputs. We thank General Motors for providing the AM50 samples and Surface Science Western for instrumentation. We thank Dr. Manas Paliwal and Prof. In-Ho Jung for performing FactSage numerical simulations.

Appendix A. Supplementary material

Supplementary data associated with this article can be found, in the online version, at http://dx.doi.org/10.1016/j.jelechem.2014.10.030.

References

[1] A. Eliezer, P.E. Krajewski, A. Ben-Artzy, N. Moskovich, Magnesium Technol. (2007) 327–330.
[2] J. Hines Forsmark, J. Boileau, D. Houston, R. Cooper, Int. J. Metalcast. Winter (2012) 15–26.
[3] D.R. Lide, CRC Handbook of Chemistry and Physics, 94th ed., Taylor & Francis, 2013.
[4] K. Lips, P. Schmutz, M. Heer, P.J. Uggowitzer, S. Virtanen, Mater. Corros. 55 (2004) 5–17.
[5] D. Sachdeva, Corros. Sci. 60 (2012) 18–31.
[6] E. Ghali, W. Dietzel, K.-U. Kainer, J. Mater. Eng. Perform. 13 (2004) 7–23.
[7] D. Eliezer, E. Aghion, F.H. Froes, Adv. Perform. Mater. 5 (1998) 201–212.
[8] H. Matsubara, Y. Ichige, K. Fujita, H. Nishiyama, K. Hodouchi, Corros. Sci. 66 (2013) 203–210.
[9] M.D. Bharadwaj, S.M. Tiwari, Y.M. Wang, V. Mani, Magnesium Technol. (2008) 389–391.
[10] A. Kielbus, T. Rzychon, R. Cibis, Manuf. Eng. 18 (2006) 135–138.
[11] S. Maddela, Y.M. Wang, A.K. Sachdev, R. Balasubramaniam, Magnesium Technol. (2009) 321–331.
[12] S. Sundarraj, M.D. Bharadwaj, S.M. Tiwari, Magnesium Technol. (2008) 329–330.
[13] M. Jönsson, D. Thierry, N. LeBozec, Corros. Sci. 48 (2006) 1193–1208.
[14] M.-C. Zhao, M. Liu, G. Song, A. Atrens, Corros. Sci. 50 (2008) 1939–1953.
[15] Y. Ma, J. Zhang, M. Yang, J. Alloys Compd. 470 (2009) 515–521.
[16] M. Danaie, R.M. Asmussen, P. Jakupi, D.W. Shoesmith, G.A. Botton, Corros. Sci. 77 (2013) 151–163.
[17] R.M. Asmussen, P. Jakupi, M. Danaie, G.A. Botton, D.W. Shoesmith, Corros. Sci. 75 (2013) 114–122.
[18] M. Jönsson, D. Persson, R. Gubner, J. Electrochem. Soc. 154 (2007) C684–C691.
[19] K. Watanabe, K. Matsuda, T. Kawabata, S. Ikeno, Adv. Mater. Res. 409 (2012) 383–386.
[20] D. Trinh, P. Dauphin, J. Mauzeroll, Anal. Chem. 84 (2012) 9899–9906.
[21] G. Williams, N. Birbilis, H.N. McMurray, Electrochem. Commun. 36 (2013) 1–5.
[22] L. Lacroix, C. Blanc, N. Pébère, B. Tribollet, V. Vivier, J. Electrochem. Soc. 156 (2009) C259–C265.
[23] A.C. Bastos, M.G. Taryba, O.V. Karavai, M.L. Zheludkevich, S.V. Lamaka, M.G.S. Ferreira, Electrochem. Commun. 12 (2010) 394–397.
[24] J. Izquierdo, L. Nagy, Á. Varga, I. Bitter, G. Nagy, R.M. Souto, Electrochim. Acta 59 (2012) 398–403.
[25] V.A. Nazarov, M.G. Taryba, E.A. Zdrachek, K.A. Andronchyk, V.V. Egorov, S.V. Lamaka, J. Electroanal. Chem. 706 (2013) 13–24.
[26] K. Tóth, G. Nagy, B.R. Horrocks, A.J. Bard, Anal. Chim. Acta 282 (1993) 239–246.
[27] A. Alvarez-Pampliega, S.V. Lamaka, M.G. Taryba, M. Madani, J. De Strycker, E. Tourwé, M.G.S. Ferreira, H. Terryn, Electrochim. Acta 61 (2012) 107–117.
[28] M. Etienne, A. Schulte, S. Mann, G. Jordan, I.D. Dietzel, W. Schuhmann, Anal. Chem. 76 (2004) 3682–3688.

[29] S.V. Lamaka, G. Knörnschild, D.V. Snihirova, M.G. Taryba, M.L. Zheludkevich, M.G.S. Ferreira, Electrochim. Acta 55 (2009) 131–141.
[30] S.V. Lamaka, O.V. Karavai, A.C. Bastos, M.L. Zheludkevich, M.G.S. Ferreira, Electrochem. Commun. 10 (2008) 259–262.
[31] R.M. Souto, A. Kiss, J. Izquierdo, L. Nagy, I. Bitter, G. Nagy, Electrochem. Commun. 26 (2012) 25–28.
[32] J. Izquierdo, L. Nagy, I. Bitter, R.M. Souto, G. Nagy, Electrochim. Acta 87 (2013) 283–293.
[33] J. Izquierdo, A. Kiss, J.J. Santana, L. Nagy, I. Bitter, H.S. Isaacs, G. Nagy, R.M. Souto, J. Electrochem. Soc. 160 (2013) C451–C459.
[34] R. Ambat, N.N. Aung, W. Zhou, Corros. Sci. 42 (2000) 1433–1455.
[35] R. Matthew Asmussen, W. Jeffrey Binns, J. Electrochem. Soc. 161 (2014) C501–C508.
[36] E. Malinowska, A. Manzoni, M.E. Meyerhoff, Anal. Chim. Acta 382 (1999) 265–275.
[37] U. Schaller, U.E. Spichiger, W. Simon, Pflügers Arch. Eur. J. Physiol. 423 (1993) 338–342.
[38] T.J. Smith, K.J. Stevenson, 4 – Reference electrodes, in: G.Z. Cynthia (Ed.), Handbook of Electrochemistry, Elsevier, Amsterdam, 2007, pp. 73–110.
[39] ASTM International, 2005.
[40] L. Danis, M.E. Snowden, U.M. Tefashe, C.N. Heinemann, J. Mauzeroll, Electrochim. Acta 136 (2014) 121–129.
[41] E. Bakker, P. Bühlmann, E. Pretsch, Chem. Rev. 97 (1997) 3083–3132.
[42] E. Bakker, M. Willer, M. Lerchi, K. Seiler, E. Pretsch, Anal. Chem. 66 (1994) 516–521.
[43] B.P. Baranwal, K. Tripathi, A.K. Singh, S. Tripathi, Spectrochim. Acta – Part A: Mol. Biomol. Spectrosc. 91 (2012) 365–369.
[44] K.J. De Almeida, T.C. Ramalho, Z. Rinkevicius, O. Vahtras, H. Ågren, A. Cesar, J. Phys. Chem. A 115 (2011) 1331–1339.
[45] X. Zhang, A. Fakler, U.E. Spichiger, Electroanalysis 10 (1998) 1174–1181.
[46] S. Bender, J. Goellner, A. Atrens, Adv. Eng. Mater. 10 (2008) 583–587.
[47] C.O.A. Nomenclature, Pure Appl. Chem. 48 (1976) 127–132.
[48] C.W. Bale, P. Chartrand, S.A. Degterov, G. Eriksson, K. Hack, R. Ben, Calphad 26 (2002) 189–228.
[49] D.H. Kang, M. Paliwal, E. Essadiqi, I.H. Jung, Magnesium Technol. (2010) 533–536.
[50] G. Song, A. Atrens, Adv. Eng. Mater. 5 (2003) 837–858.